IEEE Access
Multidisciplinary ⋮ Rapid Review ⋮ Open Access Journal

Received December 2, 2021, accepted December 21, 2021, date of publication December 24, 2021,
date of current version January 4, 2022.

Digital Object Identifier 10.1109/ACCESS.2021.3138631

Spectro-Dynamic MRI: Characterizing Mechanical Systems on a Millisecond Scale

MAX H. C. VAN RIEL[1,2,3], NIEK R. F. HUTTINGA[1,2], AND ALESSANDRO SBRIZZI[1,2]

[1]Division of Imaging & Oncology, Department of Radiotherapy, University Medical Center Utrecht, 3584 CX Utrecht, The Netherlands
[2]Center for Image Sciences, Computational Imaging Group for MR Diagnostics & Therapy, University Medical Center Utrecht, 3584 CX Utrecht, The Netherlands
[3]Department of Biomedical Engineering, Eindhoven University of Technology, 5612 AZ Eindhoven, The Netherlands

Corresponding authors: Max H. C. van Riel (m.h.c.vanriel-3@umcutrecht.nl) and Alessandro Sbrizzi (a.sbrizzi@umcutrecht.nl)

ABSTRACT Measuring in vivo dynamics can yield valuable information for studying the functioning of the cardiovascular or the musculoskeletal system and for the diagnosis of related diseases. MRI is a powerful medical imaging modality, but it shows severe limitations when dealing with motion at high spatial and temporal resolutions. In this work, a method called spectro-dynamic MRI is proposed, which can identify dynamical information directly from k-space data. It combines a measurement model, relating the measured data in k-space to the displacement fields, and a dynamical model, introducing prior knowledge about the dynamics of a system. The data sampling process is tailored to compute spatial and temporal derivatives in the spectral domain at a high temporal resolution. Preliminary results from four simple pendulum setups for which the dynamics are explicitly known show that spectro-dynamic MRI can estimate motion fields from heavily undersampled data on a millisecond timescale. Furthermore, the length of the pendula and the stiffness of the spring can be identified as the dynamical system's parameters, giving additional information about the systems under investigation.

INDEX TERMS Dynamic imaging, dynamical system identification, magnetic resonance imaging, spectro-dynamic MRI.

I. INTRODUCTION

The human body is a dynamical system. Its performance is not only determined by its static anatomy, but also by its functioning in a dynamic setting. One specific example of a dynamic organ is the heart. More than 26 million people suffer from heart failure worldwide, and its prevalence is increasing [1]. The most widely used parameter to diagnose heart failure is left ventricular ejection fraction, measured using echocardiography [2]. Moreover, myocardial strain can give important additional information in the prognosis of several cardiac diseases [3]. Being able to infer time-resolved dynamic information of the heart could provide valuable information for the diagnosis and understanding of arrhythmia and heart failure.

Another example of a biomechanical system is the musculoskeletal system. Conditions related to muscles and joints can cause long-term pain, and a large portion of the population suffers from musculoskeletal conditions [4]. Time-resolved dynamic imaging is a valuable tool to investigate the loads and motion of joints [5].

Magnetic resonance imaging (MRI) is a medical imaging modality that provides excellent soft-tissue contrast, making it an ideal candidate for imaging organs such as the heart or other muscles. Furthermore, MRI can obtain 3D information and does not involve ionizing radiation. However, a major drawback of MRI in its current form is that it is a relatively slow modality, complicating the analysis of dynamics at a combined high spatial and temporal resolution. This limitation is caused by the data acquisition process for conventional MR images. The measurements are sampled in the spectral domain, called k-space. Typically, the k-space is sampled line by line, where the acquisition of one line is called a readout [6]. Image reconstruction by the Fourier transform requires a fully sampled k-space, for which many readouts and thus long acquisition times are needed. This becomes even more problematic when adding a third spatial or a temporal dimension, which makes inferring time-resolved 3D dynamic information extremely challenging.

Several techniques exist to accelerate MRI acquisitions for imaging dynamic systems such as the heart [7]. The first

The associate editor coordinating the review of this manuscript and approving it for publication was Gang Wang.

option is to use real-time imaging [8], [9], a technique that acquires all data in a single heartbeat. However, the resulting images suffer from reduced image quality, and acquiring 3D images is not possible with this technique. Another approach is to use gated imaging [10], [11], where the acquisition is segmented such that all measurements originate from the same phase of the cardiac motion. This requires that the motion is periodic, which is problematic for patients with arrhythmia. Furthermore, addressing respiratory motion requires additional motion correction strategies.

Alternatively, the number of required samples can be reduced to accelerate data acquisition. However, this will introduce undersampling artifacts when no additional prior information is included in the reconstruction. Parallel imaging is a technique that uses the sensitivities of the receive coils to remove the aliasing in the undersampled images [12], [13]. Another option is to assume that the images are sparse in a certain domain, which is used as prior knowledge in compressed sensing approaches [14], [15], while low-rank approaches place constraints on the rank of the data [16]. Non-Cartesian sampling of k-space is often used, as it shows robustness against motion artifacts [17] and can allow self-navigation [18]. Together, these techniques allow for the reconstruction of a dynamic sequence of images [19]–[22]. Information about motion fields can additionally be used to create images free of motion artifacts [23]. For an overview of the artifacts caused by motion and how to deal with them, we refer to [18].

The methods described thus far have in common that they try to reconstruct images at a high temporal resolution from which dynamical information can be derived, or use motion correction during image reconstruction. However, some dynamics can also be estimated directly from spectral data, removing the requirement of a fully sampled k-space at every point in time. A recently developed method called MR-MOTUS [24], [25] has shown that it is possible to reconstruct motion fields directly from highly undersampled k-space data. While this method does provide motion fields at a high temporal resolution, it does not identify the parameters of the dynamical system under investigation.

In this work, we develop spectro-dynamic MRI as a method to probe time-resolved dynamic information using MRI data. Two models are combined to identify the dynamics of a system. The first model is a measurement model, providing a relation between the displacements of a moving object and the measured magnetization in the spectral domain. This model acts as a data consistency term and can reconstruct the dynamics from fully sampled data. The second model is a dynamical model, which is introduced to deal with undersampled data by adding prior knowledge about the dynamics. This dynamical model is based on the partial differential equation (PDE), describing the equations of motion for the system under investigation. Together with the measurement model, the motion fields can thus be reconstructed at a high spatial and temporal resolution. Additionally, the dynamical model allows for the reconstruction of the dynamical system parameters, which give information about the material properties of the scanned object.

Both models contain spatial and temporal derivatives. A properly tailored sampling strategy is used to infer these fundamental properties of dynamical systems. This can be done in real time by working with measurements in the spectral domain. Spatial derivatives can be conveniently calculated in k-space through multiplications with spatial frequencies. For the temporal derivatives, finite differences can be used, which require a small time step to be accurate. By using the measurements in the spectral domain, no image reconstruction is involved. This allows for a reduction of the time interval to just a few milliseconds.

This work starts with the theoretical derivation of the spectro-dynamic MRI framework. The measurement model is derived and converted to the spectral domain. Subsequently, four different dynamical systems with increasing levels of complexity are used to validate our approach. To measure these systems in a 1.5T MRI scanner, an experimental setup is created. Finally, the performance of the spectro-dynamic MRI model with highly undersampled data is investigated, showing that our proposed method can correctly reconstruct motion fields and dynamical parameters even with only two samples per readout.

II. THEORY

A. SIGNAL ACQUISITION

In an MRI experiment, the complex transverse magnetization in the spatial domain $m(\mathbf{r}, t) \in \mathbb{C}$ depends on the spatial location $\mathbf{r} \in \mathbb{R}^d$ and time t. The number of spatial dimensions is indicated by d. By applying linear gradient magnetic fields to the static magnetic field inside the scanner, this signal can be sampled in the spectral domain at the spatial frequencies $\mathbf{k} \in \mathbb{R}^d$ [6]. The spatial and spectral domains are related through the Fourier transform:

$$M(\mathbf{k}, t) = \mathcal{F}\left(m(\mathbf{r}, t)\right) = \int_{\mathbb{R}^d} m(\mathbf{r}, t) e^{-i2\pi \mathbf{k}\cdot\mathbf{r}} \, d\mathbf{r}, \quad (1)$$

$$m(\mathbf{r}, t) = \mathcal{F}^{-1}\left(M(\mathbf{k}, t)\right) = \int_{\mathbb{R}^d} M(\mathbf{k}, t) e^{i2\pi \mathbf{k}\cdot\mathbf{r}} \, d\mathbf{k}. \quad (2)$$

Note that variables in the spatial domain are indicated with lower case symbols, while upper case symbols are used for the spectral domain. Vectors are indicated in bold font.

In conventional MRI, the measurements in the spectral domain $M(\mathbf{k}, t)$ are reconstructed to image data $m(\mathbf{r}, t)$ by using the inverse discrete Fourier transform, thereby approximating (2). Since the signal contribution of one specific voxel affects the whole k-space, and each sample in k-space contains information about the complete field of view in the image domain, the k-space must be fully sampled to prevent undersampling artifacts in the reconstructed image.

The goal of spectro-dynamic MRI is to infer the dynamics of a system as well as identify its dynamical parameters. To do this, the dynamics can be modeled with spatial and temporal derivatives. As will be explained in Section III-C, these temporal derivatives can be estimated using finite differences.

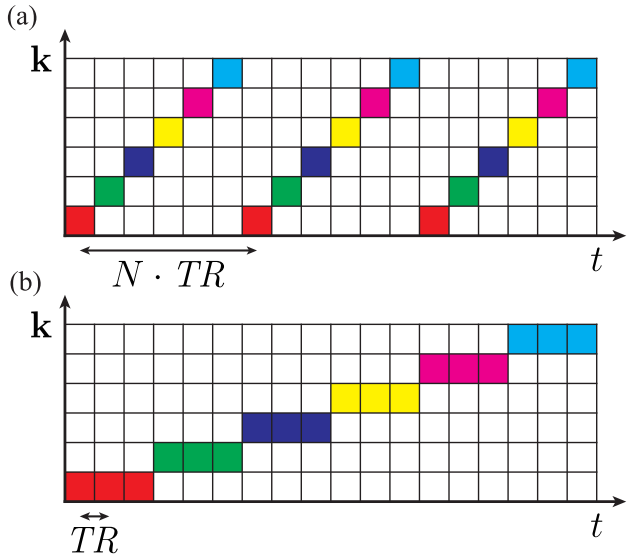

FIGURE 1. (a) Sampling pattern as used in conventional MRI. Each colored square indicates one readout, separated in time by the repetition time (*TR*). The vertical axis and the colors represent the different spatial frequencies that need to be sampled to get a fully sampled k-space (the phase-encoding steps for a Cartesian acquisition). With every readout, a different line in k-space is sampled. Thus, after N readouts ($N = 6$ in this schematic illustration), an image can be reconstructed. Typically, N is in the order of several thousand repetitions for a 3D acquisition. (b) Sampling pattern as used in spectro-dynamic MRI. The same readout line is repeated N_{rep} times (3 in this case) before different k-space frequencies are sampled. This greatly reduces the time difference Δt between the acquisition of the same data point in k-space (from $N \cdot TR$ to $1 \cdot TR$), thereby allowing the computation of temporal derivatives through finite differences.

If one would use the measured data in the spatial domain, this would require the image values $m(\mathbf{r}, t)$ and $m(\mathbf{r}, t + \Delta t)$ to be available at some spatial location $\mathbf{r}$. Since these images must first be reconstructed, this also means that two fully sampled k-spaces at these time points need to be available. Therefore, Δt cannot be smaller than the time it takes to sample a complete k-space (Fig. 1(a)), which for 3D acquisitions is in the order of seconds. This low temporal resolution leads to motion artifacts in the reconstruction.

Instead, we propose to use the data in the spectral domain directly. To estimate temporal derivatives using finite differences, we need the measurements $M(\mathbf{k}, t)$ and $M(\mathbf{k}, t + \Delta t)$ in k-space. Since the intermediate reconstruction step is no longer required, Δt can be as short as the repetition time TR, which is in the order of milliseconds (Fig. 1(b)). Thus, the temporal resolution of the measurements can be improved by using heavily undersampled k-spaces at successive points in time.

B. SPECTRO-DYNAMIC MRI MODEL

The dynamics of a moving and possibly deforming object can be described by a displacement field $\mathbf{u}(\mathbf{r}, t) \in \mathbb{R}^d$, with its Fourier transform $\mathbf{U}(\mathbf{k}, t)$. A measurement model G will be used to describe the relation between this displacement field and the measurements $M(\mathbf{k}, t)$ in the spectral domain:

$$G(M(\mathbf{k}, t), \mathbf{U}(\mathbf{k}, t), \mathbf{k}) = 0. \tag{3}$$

Here, G is written in implicit form. For an explicit example, see (10) as derived in Section II-C.

When fully sampled data is available, this measurement model is sufficient to reconstruct the unknown displacement field. In this case, (3) can be inverted, for example by reconstructing all images and applying image registration to find the displacements. However, acquiring time-resolved fully-sampled k-space data in 3D is extremely challenging. Therefore, the measured data will be undersampled, turning the inversion of (3) from a well-posed problem into an ill-posed problem. Therefore, additional information about the system under investigation needs to be provided. The measurement model G will be used in combination with a dynamic model F which provides a priori knowledge about the dynamics of the system. This dynamical model also allows for the reconstruction of a set of dynamical parameters, yielding more information about the system's dynamical properties.

The dynamics of a system can be modeled with a PDE. In general, this PDE is a function of the displacement field, its spatial and temporal derivatives, and a set of dynamical parameters $\boldsymbol{\theta}(\mathbf{r})$, which can be spatially dependent. Like the measurement model, this dynamical model can also be converted to the spectral domain, resulting in:

$$F(\mathbf{U}(\mathbf{k}, t), \boldsymbol{\Theta}(\mathbf{k}), \mathbf{k}) = 0. \tag{4}$$

The specific form for (4) depends on the dynamical system that is being investigated. See (12) and Section III-D for more details about the dynamical systems used in this study.

Given the measurement model G and the dynamical model F, the dynamics as described by the displacement field and the dynamical parameters can be reconstructed. One option is to minimize the L^2 norm of the error of one model while using the other model as an equality constraint. However, it is important to note that both (3) and (4) will be subject to imperfections. Measurement noise will introduce errors in the measurement model, while model imperfections will result in a difference between the observed dynamics and the modeled dynamics. Therefore, a single optimization problem will be solved, where we use the dynamical model as a penalty term (or regularizer) on the measurement model [26]:

$$\min_{\mathbf{U}, \boldsymbol{\Theta}} \|G(M, \mathbf{U}, \mathbf{k}, t)\|_2^2 + \lambda \|F(\mathbf{U}, \boldsymbol{\Theta}, \mathbf{k}, t)\|_2^2. \tag{5}$$

Here, λ is introduced as a trade-off parameter that changes the amount of regularization of the dynamical model on the measurement model. If $\lambda = 0$, only the measurement model is used. This will allow for the reconstruction of the displacement field $\mathbf{U}$ in case of a fully sampled acquisition. However, the solution will be more sensitive to noise, and no dynamical parameters can be estimated. Increasing λ will increase the robustness to measurement noise, but it will create a bias towards the dynamics included in the dynamical model. Ultimately, when λ goes to infinity, the reconstructed solution is equivalent to the one obtained when the dynamical model is used as an equality constraint on the measurement model. In this case, any model imperfections in the dynamical

model will no longer be corrected, and any dynamics not included in the dynamical model will no longer be reconstructed. Therefore, it is important to find a suitable value for λ which balances the residuals of both models.

C. MEASUREMENT MODEL

The measurement model describes how the measured magnetization changes due to the dynamics of the measured system. We will assume that the magnetization is in steady state, that the receive and excitation fields are homogeneous or very smooth (which is reasonable to assume at the targeted field strength of 1.5T [24]), and that short readouts are used such that T_1 and T_2 effects during readout can be ignored. Under these assumptions, the magnetization of an object is conserved. Therefore, the derivation of the measurement model is similar to the one used for the conservation of mass when modeling fluid mechanics [27]. This results in a differential equation, describing the conservation of magnetization using the continuity equation, as derived in Appendix A:

$$\frac{\partial}{\partial t}m(\mathbf{r},t)+\nabla m(\mathbf{r},t)\cdot\mathbf{v}(\mathbf{r},t)+m(\mathbf{r},t)\big[\nabla\cdot\mathbf{v}(\mathbf{r},t)\big]=0. \tag{6}$$

To couple this measurement model with the dynamical model, we will need to introduce the displacements $\mathbf{u}(\mathbf{r},t)$ into our measurement model. The displacement field is defined in the Eulerian description (see Appendix B), where the displacement of a particle at a spatial location $\mathbf{r}$ in the current configuration is the difference between that location and the original location $\mathbf{r}_0$ of the same particle in some reference configuration:

$$\mathbf{u}(\mathbf{r},t)=\mathbf{r}-\mathbf{r}_0(\mathbf{r},t). \tag{7}$$

Note that the initial location is a dependent variable in this notation. To describe (6) in terms of (7), we assume that the velocity field is the temporal derivative of the displacement field:

$$\mathbf{v}(\mathbf{r},t)\approx\frac{\partial}{\partial t}\mathbf{u}(\mathbf{r},t). \tag{8}$$

This assumption is valid as long as the displacement field is smooth across space (see Appendix B). Combining (6) and (8) gives us the measurement model in the spatial domain:

$$\frac{\partial}{\partial t}m(\mathbf{r},t)+\nabla m(\mathbf{r},t)\cdot\frac{\partial}{\partial t}\mathbf{u}(\mathbf{r},t)+m(\mathbf{r},t)\left[\nabla\cdot\frac{\partial}{\partial t}\mathbf{u}(\mathbf{r},t)\right]=0. \tag{9}$$

In MRI, the measurements are sampled in the spectral domain. If we would use (9) directly, we would have to reconstruct the image data $m(\mathbf{r},t)$ from the measured k-space data $M(\mathbf{k},t)$. The temporal resolution can be increased by directly using the spectral data, removing the need for an image reconstruction step. To do so, we must transform (9) to the spectral domain. This can be done using the properties of the Fourier transform, resulting in:

$$\frac{\partial}{\partial t}M(\mathbf{k},t)+i2\pi\sum_{j=1}^{d}k_jM(\mathbf{k},t)*\frac{\partial}{\partial t}U_j(\mathbf{k},t)+i2\pi\sum_{j=1}^{d}M(\mathbf{k},t)*k_j\frac{\partial}{\partial t}U_j(\mathbf{k},t)=0. \tag{10}$$

III. METHODS

A. DYNAMICAL MODEL

In this work, we study the dynamics of systems consisting of discrete particles and with n degrees of freedom. For example, a single particle that is free to move in both the x- and y-direction has two degrees of freedom. Systems with nonconservative or external forcing terms will be excluded. The (linearized) equations of motion of these systems can be described by a second-order differential equation [28]–[30]:

$$M_D(\boldsymbol{\theta})\frac{d^2}{dt^2}\mathbf{q}(t)+K_D(\boldsymbol{\theta})\mathbf{q}(t)=\mathbf{0}. \tag{11}$$

Here, $\mathbf{q}(t)\in\mathbb{R}^n$ are the generalized coordinates for each of the n degrees of freedom, $M_D=M_D^T\in\mathbb{R}^{n\times n}$ and $K_D=K_D^T\in\mathbb{R}^{n\times n}$ are respectively the mass and stiffness matrix, which depend on the dynamical parameters $\boldsymbol{\theta}$. Which parameters are included in $\boldsymbol{\theta}$ depend on the dynamical model, and are specified in Section III-D.

None of the quantities in (11) are dependent on $\mathbf{r}$. The spatial dependencies are implicitly included in the model, as each generalized coordinate corresponds to one part of the moving system, with its own location in space. It is assumed that a coordinate system is chosen such that $\mathbf{q}=\mathbf{0}$ is the equilibrium position. The generalized coordinates are connected to the displacement field $\mathbf{u}(\mathbf{r},t)$ through a set of basis functions, as described in Section III-B.

Note that despite the names of M_D and K_D, this model is not only applicable to mass-spring systems. Any nonlinear system, such as a swinging pendulum, can also be described by (11) as long as the displacement from equilibrium is small. Furthermore, (11) can directly be used in the spectral domain, since neither $\mathbf{r}$ nor $\mathbf{k}$ appear explicitly.

The dynamical model is premultiplied with $(M_D(\boldsymbol{\theta}))^{-1}$. This results in a better scaling of the parameters and prevents the optimization from converging towards parameters for which the mass matrix is very small. Using the matrix $\Omega_D(\boldsymbol{\theta})=\big(M_D(\boldsymbol{\theta})\big)^{-1}K_D(\boldsymbol{\theta})$, whose eigenvalues are the squared natural frequencies of the system, the dynamical model can alternatively be written as:

$$\frac{d^2}{dt^2}\mathbf{q}(t)+\Omega_D(\boldsymbol{\theta})\mathbf{q}(t)=\mathbf{0}. \tag{12}$$

B. BASIS FUNCTIONS

The displacement field $\mathbf{u}(\mathbf{r},t)$ is defined at every spatial location, while the dynamical systems only have a limited number of degrees of freedom. Therefore, we can reduce the dimensionality of our optimization problem (5) by using a

set of n spatially varying basis functions. We assume that, by using the right choice of basis functions, a relation between the displacement field $\mathbf{u}(\mathbf{r}, t)$ and the i^{th} generalized coordinate $q_i(t)$ can be defined by the i^{th} basis function $\boldsymbol{\xi}_i(\mathbf{r}) \in \mathbb{R}^d$:

$$\mathbf{u}(\mathbf{r}, t) = \sum_{i=1}^{n} \boldsymbol{\xi}_i(\mathbf{r}) q_i(t). \tag{13}$$

Next, (13) can be converted to the spectral domain since the Fourier transform is a linear transformation:

$$\mathbf{U}(\mathbf{k}, t) = \sum_{i=1}^{n} \boldsymbol{\Xi}_i(\mathbf{k}) q_i(t). \tag{14}$$

C. DISCRETIZATION

As described in Section II-A, we can sample k-space at a high temporal resolution. This allows for the approximation of the temporal derivatives in (10) and (12) using finite differences. Using (14), the first temporal derivatives in (10) using finite differences are defined as:

$$\frac{\partial}{\partial t} M(\mathbf{k}, t_i) \approx \frac{M(\mathbf{k}, t_{i+1}) - M(\mathbf{k}, t_{i-1})}{2\Delta t}, \tag{15}$$

$$\frac{\partial}{\partial t} \mathbf{U}(\mathbf{k}, t_i) \approx \sum_{i=1}^{n} \boldsymbol{\Xi}_i(\mathbf{k}) \frac{q_i(t_{i+1}) - q_i(t_{i-1})}{2\Delta t}. \tag{16}$$

Applying finite differences to the second temporal derivative in (12) gives:

$$\frac{d^2}{dt^2} \mathbf{q}(t_i) \approx \frac{\mathbf{q}(t_{i+1}) - 2\mathbf{q}(t_i) + \mathbf{q}(t_{i-1})}{\Delta t^2}. \tag{17}$$

If we have measurements from p different time points, and n degrees of freedom, we can concatenate all vectors $\mathbf{q}(t_i)$ for $i = 1 \ldots p$ to form one vector $\mathbf{q} \in \mathbb{R}^{np}$ which contains all generalized coordinates at every time point. By combining (10), (12), and (15)–(17), we can rewrite both models as a linear expression in $\mathbf{q}$:

$$G = i2\pi \big(\mathcal{S}\mathcal{T}(\mathcal{K}\mathbf{m}) + \mathcal{T}(\mathbf{m})\mathcal{S}\mathcal{K}\big)\mathcal{D}_t \mathcal{B}\mathbf{q} + \mathcal{D}_t \mathbf{m} = \mathbf{0}, \tag{18}$$

$$F = \big(\mathcal{D}_{tt} + I_p \otimes \Omega_D(\boldsymbol{\theta})\big)\mathbf{q} = \mathbf{0}. \tag{19}$$

Here:

- $\mathbf{q} \in \mathbb{R}^{np}$ is a vector with all generalized coordinates at every time point;
- $\mathbf{m} \in \mathbb{C}^{Np}$ is a vector with all measured data;
- $\mathcal{D}_t \in \mathbb{R}^{Np \times Np}$ is the first-order finite difference operator in the temporal dimension;
- $\mathcal{B} \in \mathbb{R}^{Np \times np}$ is a matrix whose columns represent the basis functions $\boldsymbol{\Xi}_i(\mathbf{k})$ evaluated at the desired k-space coefficients, thereby converting the generalized coordinates to the displacement field according to (14);
- $\mathcal{K} \in \mathbb{R}^{Npd \times Np}$ is a matrix that performs multiplication with the k-space coefficients for the spatial derivatives;
- $\mathcal{S} \in \{0, 1\}^{Np \times Npd}$ performs a summation over the spatial dimensions;
- $\mathcal{T}(\cdot)$ creates a Toeplitz matrix such that $\mathcal{T}(\mathbf{f})\mathbf{g} = \mathbf{f} * \mathbf{g}$;
- $\mathcal{D}_{tt} \in \mathbb{R}^{np \times np}$ is the second-order finite difference operator in the temporal dimension;

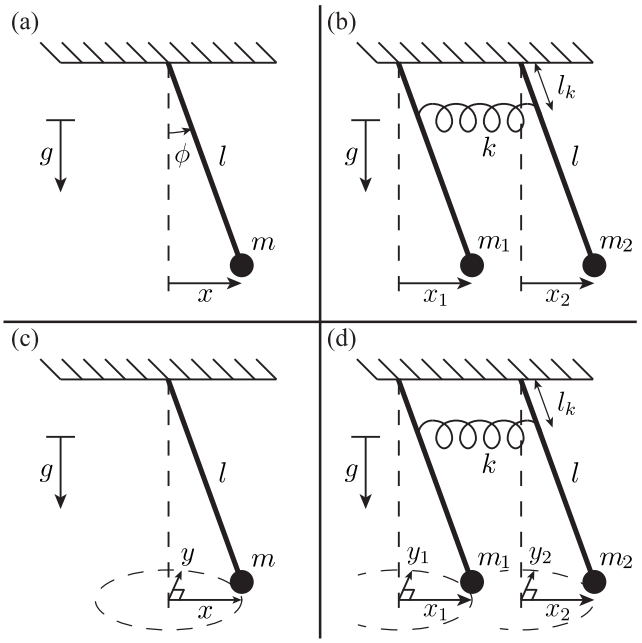

FIGURE 2. Schematic overviews of the four different dynamical systems: (a) simple pendulum, (b) coupled pendula, (c) spherical pendulum, and (d) coupled spherical pendula. All pendula have length l and mass m, m_1, or m_2. They are subject to a gravitational force in the vertical direction, with gravitational acceleration g. The position of each pendulum is described by two orthogonal coordinates x and y, both in the horizontal plane. Systems (b) and (d) also contain a spring, attached to the two pendula at a distance l_k from the pivot point, with spring constant k.

- I_p is the $p \times p$ identity matrix;
- $\otimes$ is the Kronecker product;
- $\Omega_D(\boldsymbol{\theta}) = \big(M_D(\boldsymbol{\theta})\big)^{-1} K_D(\boldsymbol{\theta})$ is an $n \times n$ matrix depending on the dynamical parameters $\boldsymbol{\theta}$.

Equations (18) and (19) can be rewritten in short notation as $G = A\mathbf{q} - \mathbf{b}$ and $F = C(\boldsymbol{\theta})\mathbf{q}$, respectively. Substituting these linear models in (5), the optimization problem can now be formulated as a regularized linear least squares problem:

$$\min_{\mathbf{q}, \boldsymbol{\theta}} \|A\mathbf{q} - \mathbf{b}\|_2^2 + \lambda \|C(\boldsymbol{\theta})\mathbf{q}\|_2^2. \tag{20}$$

D. EXPERIMENTAL SETUPS

To test the validity of the derived spectro-dynamical model, we performed several experiments. Different dynamical systems were used, with increasing degrees of complexity. The variables used in these equations are shown in Table 1.

1) SIMPLE PENDULUM

To start, a simple pendulum with one degree of freedom (Fig. 2(a)) was considered. Using the angle ϕ the pendulum makes with respect to the vertical position, the differential equation of this system is:

$$ml\frac{d^2\phi}{dt^2} + mg\sin\phi = 0. \tag{21}$$

The dynamics of this system can be linearized around the stable equilibrium $\phi = 0$, introducing an error larger than

TABLE 1. Variables used in the dynamical equations.

Symbol	Description [unit]
g	Gravitational acceleration $\left[\text{m/s}^2\right]$
k	Spring stiffness [N/m]
l	Pendulum length [m]
l_k	Spring attachment distance [m]
$m_{[1,2]}$	Pendulum mass [kg]
$\boldsymbol{\theta}$	Dynamical parameters
$\tau_{[1,2]}$	$= \frac{kl_k^2}{m_{[1,2]}l^2}$ $\left[(\text{rad/s})^2\right]$
ϕ	Pendulum angle [rad]
ω	Natural frequency [rad/s]

1% only if ϕ is more than 14 degrees. This small-angle approximation results in a differential equation analogous to the one of a mass connected to a spring. Written in the format of (11), this results in:

$$\begin{aligned} n &= 1, \\ \mathbf{q} &= \left[x\right], \\ M_D(\boldsymbol{\theta}) &= \left[l\right], \\ K_D(\boldsymbol{\theta}) &= \left[g\right]. \end{aligned} \tag{22}$$

Since the gravitational acceleration g is fixed to 9.81 m/s^2, the only remaining unknown dynamical parameter is the length of the pendulum l:

$$\boldsymbol{\theta} = \left[l\right]. \tag{23}$$

Note that the polar coordinate ϕ has been replaced by the Cartesian coordinate x. Since there is only one degree of freedom, there is only a single basis function, which has a constant value of 1 over the entire spatial domain:

$$\boldsymbol{\xi}_1(\mathbf{r}) = 1 \qquad \forall\, \mathbf{r}. \tag{24}$$

2) COUPLED PENDULA

Two simple pendula, as described by (21), can be coupled together with a spring to form a slightly more complicated dynamical system (Fig. 2(b)). This coupled oscillator shows nonlinear dynamics. However, we can again linearize these equations using the small-angle approximation and rewrite them in terms of the Cartesian coordinates x_1 and x_2 of both pendula. The system then becomes equivalent to two masses connected with three springs, as described by:

$$\begin{aligned} n &= 2, \\ \mathbf{q} &= \begin{bmatrix} x_1 \\ x_2 \end{bmatrix}, \\ M_D(\boldsymbol{\theta}) &= \begin{bmatrix} m_1 l^2 & 0 \\ 0 & m_2 l^2 \end{bmatrix}, \\ K_D(\boldsymbol{\theta}) &= \begin{bmatrix} m_1 gl + kl_k^2 & -kl_k^2 \\ -kl_k^2 & m_2 gl + kl_k^2 \end{bmatrix}. \end{aligned} \tag{25}$$

Here, x_1 and x_2 are respectively the x-coordinates of the first and second pendulum, m_1 and m_2 are their masses, and k is the spring constant. Both pendula have the same length l, and the spring is attached at a distance l_k from the pivot point.

In total there are six unknown dynamical parameters in (25). However, because of the structure of the matrices, only three parameters can be estimated. Again, the gravitational acceleration g is fixed to 9.81 m/s^2 such that the length l can be estimated. The remaining parameters are captured by τ_1 and τ_2, which are defined as:

$$\tau_1 = \frac{kl_k^2}{m_1 l^2}, \tag{26}$$

$$\tau_2 = \frac{kl_k^2}{m_2 l^2}. \tag{27}$$

This leaves only three unknown parameters to be estimated:

$$\boldsymbol{\theta} = \left[l, \tau_1, \tau_2\right]. \tag{28}$$

It is assumed that the maximum displacement of each pendulum is not larger than half the distance between the pivot points, such that each pendulum is confined to a separate half-plane. Two basis functions are used, one for each pendulum:

$$\boldsymbol{\xi}_1(\mathbf{r}) = 1 - H_x(\mathbf{r}), \quad \boldsymbol{\xi}_2(\mathbf{r}) = H_x(\mathbf{r}), \tag{29}$$

where $H_x(\mathbf{r})$ is the Heaviside step function in the x-direction:

$$H_x(\mathbf{r}) = \begin{cases} 0, & \text{for } x < 0, \\ 1, & \text{for } x \geq 0. \end{cases} \tag{30}$$

3) SPHERICAL PENDULUM

If a simple pendulum can swing in two directions, it is called a spherical pendulum since its tip traces the surface of a sphere (Fig. 2(c)). The dynamics of this system can be described in spherical coordinates by two coupled, nonlinear differential equations [31]. Again, these equations must be linearized around the equilibrium. For small displacements, this system is analogous to a single mass connected to two identical springs placed along the x- and y-directions:

$$\begin{aligned} n &= 2, \\ \mathbf{q} &= \begin{bmatrix} x \\ y \end{bmatrix}, \\ M_D(\boldsymbol{\theta}) &= \begin{bmatrix} l & 0 \\ 0 & l \end{bmatrix}, \\ K_D(\boldsymbol{\theta}) &= \begin{bmatrix} g & 0 \\ 0 & g \end{bmatrix}. \end{aligned} \tag{31}$$

Again, the length of the pendulum is the only unknown parameter:

$$\boldsymbol{\theta} = \left[l\right]. \tag{32}$$

Two basis functions were used for the displacement in the x- and y-direction respectively:

$$\begin{aligned} \boldsymbol{\xi}_1(\mathbf{r}) &= \begin{bmatrix} 1 \\ 0 \end{bmatrix} \quad \forall\, \mathbf{r}, \\ \boldsymbol{\xi}_2(\mathbf{r}) &= \begin{bmatrix} 0 \\ 1 \end{bmatrix} \quad \forall\, \mathbf{r}. \end{aligned} \tag{33}$$

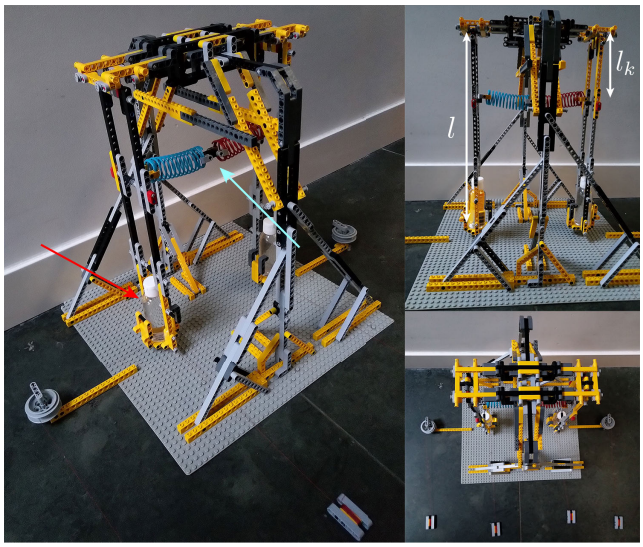

FIGURE 3. Experimental setup as used in all experiments. Two spherical pendula of length l were connected with a spring (light blue arrow), attached at distance l_k from the pivot point. The complete setup was made from plastic. At the tip of each pendulum, a gel-filled glass vial was placed (red arrow). Thin cotton strings allowed the operation of the pendula from a distance.

4) COUPLED SPHERICAL PENDULA

Finally, we can couple two spherical pendula together by placing a spring between the two swinging rods (Fig. 2(d)). This results in a system with four degrees of freedom. The linearized differential equations are equivalent to the ones for two masses, each connected to two orthogonal springs, with another spring connecting the two masses:

$$n = 4,$$
$$\mathbf{q} = \begin{bmatrix} x_1 \\ y_1 \\ x_2 \\ y_2 \end{bmatrix},$$
$$M_D(\boldsymbol{\theta}) = \begin{bmatrix} m_1 l^2 & 0 & 0 & 0 \\ 0 & m_1 l^2 & 0 & 0 \\ 0 & 0 & m_2 l^2 & 0 \\ 0 & 0 & 0 & m_2 l^2 \end{bmatrix},$$
$$K_D(\boldsymbol{\theta}) = \begin{bmatrix} m_1 g l + k l_k^2 & 0 & -k l_k^2 & 0 \\ 0 & m_1 g l & 0 & 0 \\ -k l_k^2 & 0 & m_2 g l + k l_k^2 & 0 \\ 0 & 0 & 0 & m_2 g l \end{bmatrix}. \tag{34}$$

The parameters τ_1 and τ_2 as described by (26) and (27) are used again, resulting in three unknown parameters:

$$\boldsymbol{\theta} = \left[l, \tau_1, \tau_2 \right]. \tag{35}$$

During reconstruction, four basis functions were used; two for the x- and y-displacements in one half of the spatial domain, and two for those in the other half:

$$\boldsymbol{\xi}_1(\mathbf{r}) = \begin{bmatrix} 1 - H_x(\mathbf{r}) \\ 0 \end{bmatrix}, \quad \boldsymbol{\xi}_2(\mathbf{r}) = \begin{bmatrix} 0 \\ 1 - H_x(\mathbf{r}) \end{bmatrix},$$
$$\boldsymbol{\xi}_3(\mathbf{r}) = \begin{bmatrix} H_x(\mathbf{r}) \\ 0 \end{bmatrix}, \quad \boldsymbol{\xi}_4(\mathbf{r}) = \begin{bmatrix} 0 \\ H_x(\mathbf{r}) \end{bmatrix}. \tag{36}$$

Again, this assumes that the masses are confined to nonintersecting half-planes.

E. DATA ACQUISITION

A setup was made using Lego (The Lego Group, Billund, Denmark) that allowed for testing all the described dynamical systems (Fig. 3). Since this construction was made entirely from plastic, it did not generate any signal during the scan that could interfere with the measurements. It consisted of two rigid arms with a pivot allowing for motion in two directions. The two pendula could additionally be coupled using a plastic spring. Since the linearization of the differential equations for the coupled systems required that the spring's orientation remains straight, the spring was attached near the top of the pendula to minimize its displacement.

At the extremity of each arm, a gel-filled glass vial (TO5, Eurospin II test system, Scotland) was placed in a vertical position (see Fig. 3), generating MR signal. Thin cotton strings with negligible weight were attached to each pendulum to allow manual operation of the pendula from outside the MRI scanner bore. The pendula were brought from equilibrium just before data acquisition started, and were able to swing freely during the measurements. By removing the second pendulum, or by not giving any initial displacement in the y-direction, all four systems as described in Section III-D could be measured using this single setup.

The experiments were performed with a 1.5T MRI scanner (Ingenia, Philips Healthcare, Best, The Netherlands). A spoiled gradient echo sequence was used with the scan parameters as reported in Table 2. The body coil was used as receive array to get a homogeneous receive sensitivity. Data acquisition was done in a horizontal 2D slice perpendicular to the orientation of the gel-filled tubes, with a Cartesian sampling pattern and a right-left readout direction. The imaging slice was placed in the middle of the tubes, such that they did not leave the slice at any point during the motion. Every readout line was repeated N_{rep} times before moving on to the next line, as in Fig. 1(b). This pattern resulted in fully sampled data along the k_x-direction, while only a single k_y frequency was sampled per readout.

F. RECONSTRUCTION

The noise in the measured (complex-valued) k-space data was smoothed out by applying a Gaussian filter with a standard deviation of 10 ms in the temporal dimension (by convolution) and 1 cm in the readout direction (by windowing the k-space). The generalized coordinates $\mathbf{q}$ and the dynamical parameters $\boldsymbol{\theta}$ were estimated by solving the optimization problem as given in (20). A suitable value for the regularization parameter λ was chosen by comparing the residuals of the measurement model and the dynamical model using the L-curve approach [32]. Since the optimization is linear in $\mathbf{q}$, variable projection (VARPRO) [33]–[35] could be used to solve for $\mathbf{q}$ and $\boldsymbol{\theta}$ separately. Thus, the generalized

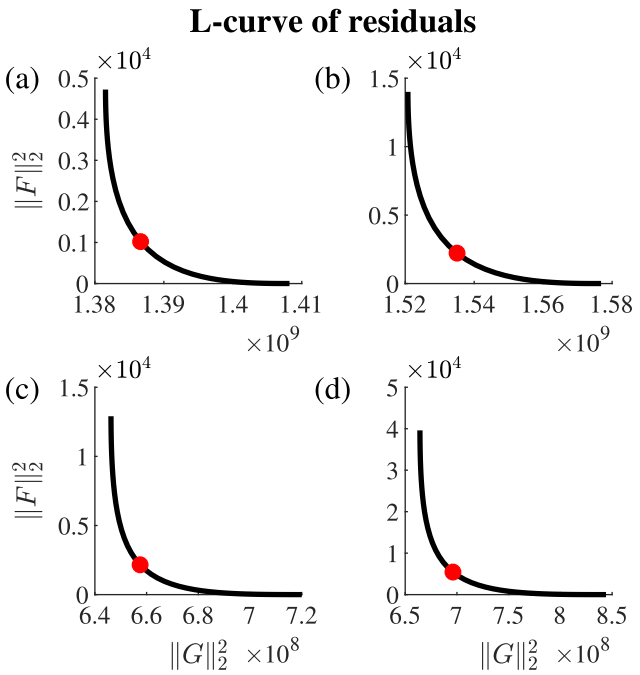

FIGURE 4. L-curves of both models' residuals for the experiments with (a) a simple pendulum, (b) coupled pendula, (c) a spherical pendulum, and (d) coupled spherical pendula. The horizontal axis is the residual of the measurement model G, while the residual of the dynamical model F is given on the vertical axes. The 61 values for λ used to create these curves ranged from 10 to 1.0×10^7, spaced evenly on a logarithmic scale. The red dot indicates the chosen value $\lambda = 5.0 \times 10^3$.

TABLE 2. Data acquisition parameters.

Parameter	Value - 1D Experiments	Value - 2D Experiments
Repetition time (TR)	4.4 ms	
Echo time (TE)	2.1 ms	
Flip angle	9 degrees	
Field of view	420 mm × 195 mm	
Slice thickness	15 mm	
Matrix size	212 × 1	212 × 12
Number of repetitions (N_{rep})	2400	100
Total number of readouts (p)	2400	1200

coordinates could be estimated efficiently using a complete orthogonal decomposition [36] as implemented in Matlab (The MathWorks Inc., Natick, MA, USA). The dynamical parameters $\boldsymbol{\theta}$ were optimized using Matlab's `lsqnonlin` function.

G. VALIDATION

To validate the estimated displacements, a 1D Fast Fourier Transform (FFT) was performed on each readout line. The maximum intensity of each glass vial was determined and, after smoothing over time, used as a reference position for that tube in the readout direction. Note that this cannot be done in the phase-encoding direction (orthogonal to the readout direction), since only one sample point in this direction is available at each repetition interval, while the measurements are fully sampled along the readout direction. This reference signal for the displacements was compared to the reconstructed displacements by calculating the root mean square error (RMSE) for the n_x generalized coordinates $q_i(t)$ in the x-direction:

$$\text{RMSE}_x = \sqrt{\frac{1}{n_x p} \sum_i \sum_{j=1}^{p} \left(q_i(t_j) - q_{i,\text{ref}}(t_j)\right)^2}. \tag{37}$$

The estimated dynamical parameters $\boldsymbol{\theta}$ were validated by taking the FFT of the reference displacements in the temporal dimension. The resulting spectrum gives the contribution of each frequency in the dynamics. The frequencies with the highest contribution should be concentrated around the natural frequencies of the system, which can be found by solving the following eigenvalue problem for ω [28]–[30]:

$$\det\left(K_D(\boldsymbol{\theta}) - \omega^2 M_D(\boldsymbol{\theta})\right) = 0. \tag{38}$$

The validation signal was zero-padded before taking the FFT, increasing the spectral resolution of the frequency spectrum. This allowed for better visibility of the frequencies corresponding to the peaks in the spectrum.

For the 2D experiments, time-resolved images were reconstructed by correcting all readout lines using the estimated displacements. Since the displacement field was piecewise constant, a convolution with the basis functions in the spectral domain was performed on the data to separate the pendula. Next, a linear phase shift corresponding to the difference between the estimated displacement and the target position was applied, after which the corrected data from the two pendula were summed together. Finally, averaging over the temporal dimension and a spatial FFT resulted in a sequence of images that could be played as a movie showing the moving phantom.

H. UNDERSAMPLING

The acquired data used so far has been fully sampled for the 1D acquisitions, and only undersampled in the phase-encode direction for the 2D experiments. In future 3D experiments, an additional dimension would have to be undersampled. To investigate the behavior of the reconstructions with even fewer available data, the readout direction was retrospectively undersampled by selecting a small subset of N samples per readout. These few points were selected symmetrically around the center of k-space (except for $N = 1$). Again, the estimated displacements in the x-direction were validated using the RMSE as given by (37). The number of samples N must be at least equal to the number of degrees of freedom n, or the measurement model is underdetermined and the displacement field can no longer be estimated.

IV. RESULTS

The L-curves of the residuals for both models can be seen in Fig. 4. For all four experiments, a regularization parameter of $\lambda = 5.0 \times 10^3$ resulted in a good trade-off by suppressing

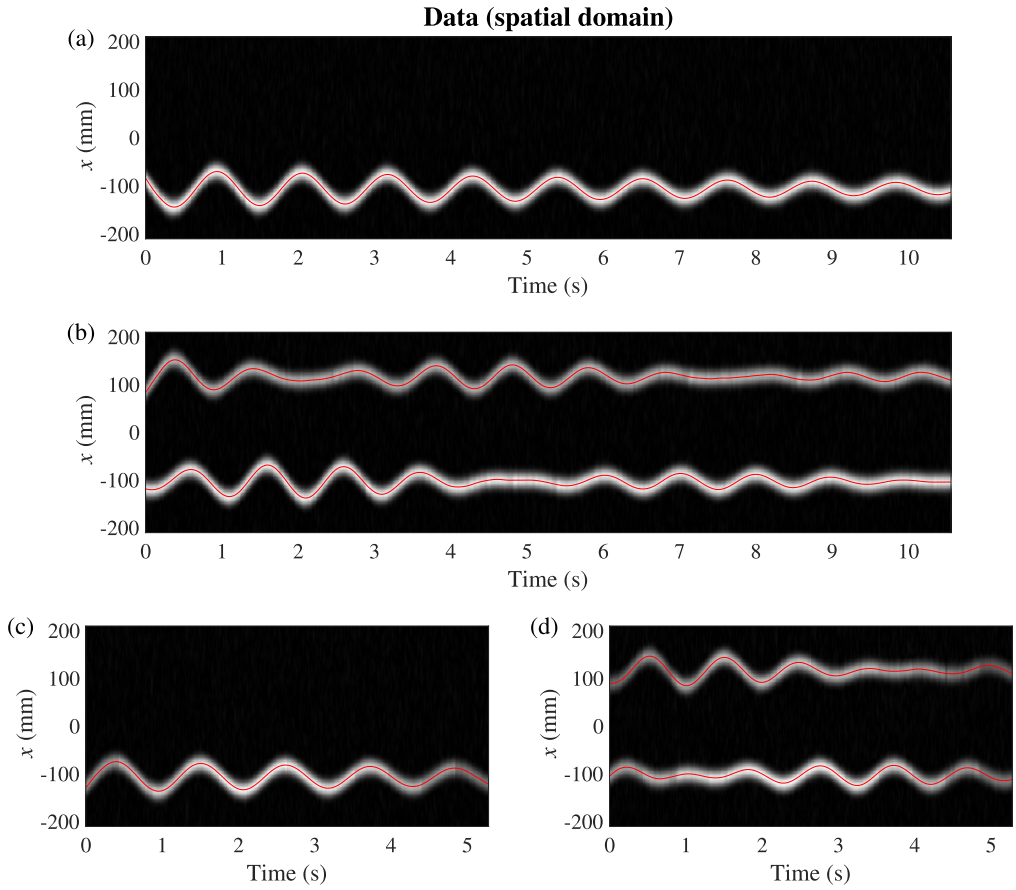

FIGURE 5. Spatial 1D FFT of all readout lines, for the experiments with (a) a simple pendulum, (b) coupled pendula, (c) a spherical pendulum, and (d) coupled spherical pendula. The maximum intensity of each tube was determined and smoothed over time to obtain the red reference lines. Note that for the 2D acquisitions in (c) and (d), only the data in the x-direction could be reconstructed. Furthermore, the contrast changes after every 100 repetitions, as the next k_y-coordinate is sampled.

noise in the measurement model, without introducing too much bias towards the dynamical model.

In Fig. 5, the spatial 1D FFT of the data can be seen. For the 1D experiments, which are fully sampled, the oscillations with one or two frequencies are clearly visible. The data of the 2D experiments can only be visualized along the x-direction, as only one k_y frequency was sampled at every point in time. Furthermore, transitions in the image contrast are visible every 100 readouts, as different k_y-coordinates were acquired. Still, this 1D reconstruction can be used to generate a reference line for the displacements in the x-direction.

The reconstructed displacements of all degrees of freedom can be seen in Fig. 6. The estimated displacements accurately follow the reference line, with a temporal resolution of one *TR* (4.4 ms). This is also evident from the RMSE_x, which is in the order of 0.1 mm for the (fully sampled) 1D acquisitions, and around 1 mm for the (undersampled) 2D acquisitions (Table 3). Note that the amplitude of the estimated displacements is gradually decreasing, even though no friction was included in the dynamical model. This shows the robustness of our method against imperfections in the dynamical model, given the right choice of λ.

TABLE 3. Reconstructed dynamical parameters.

Experiment	RMSE_x [mm]	l [mm]	τ_1 [1] [(rad/s)^2]	τ_2 [2] [(rad/s)^2]
Simple Pendulum	0.43	303	N.A.	N.A.
Coupled Pendula	0.35	284	7.72	7.37
Spherical Pendulum	1.3	302	N.A.	N.A.
Coupled Spherical Pendula	1.1	301	7.72	8.06

[1] $\tau_1 = (kl_k^2)/(m_1 l^2)$.
[2] $\tau_2 = (kl_k^2)/(m_2 l^2)$.

For the displacements in the y-direction, no reference line is available. From the theoretical model, a harmonic oscillation with a slowly decreasing amplitude due to friction would be expected in this direction. However, as can be seen in Fig. 6(c) and 6(d), the amplitude of the reconstructed displacements is not constant, nor is it gradually decreasing.

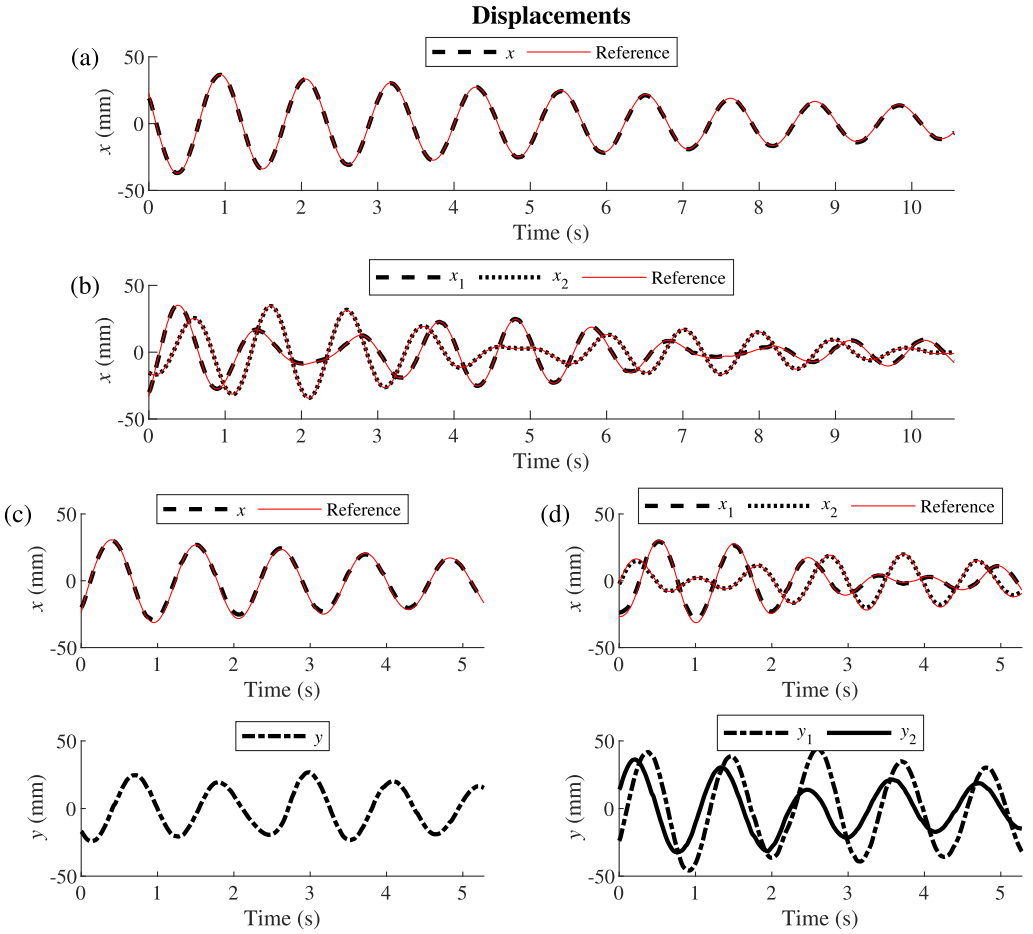

FIGURE 6. The estimated displacements. The black lines indicate the estimated displacements for the experiments with (a) a simple pendulum, (b) coupled pendula, (c) a spherical pendulum, and (d) coupled spherical pendula. For the 2D acquisitions in (c) and (d), the x- and y-displacements are plotted separately. The red line is the reference line as computed from the spatial 1D FFTs of the readouts, as shown in Fig. 5.

By correcting every readout line using the estimated displacements, a series of time-resolved images could be reconstructed of the coupled spherical pendulum experiment at a temporal resolution of 4.4 ms. The result (Video S1) can be found as supplementary material on `https://ieeexplore.ieee.org`. Note that the images suffer from severe artifacts in the phase-encode direction due to the high undersampling factor. Better encoding schemes could possibly solve this problem.

The estimated dynamical parameters are given in Table 3. The length of the pendulum is consistently estimated to be around 30 cm. The actual distance between the pivot point and the center of the tube is 32 cm. However, care must be taken when comparing these values, as the pendulum is not a point mass. Additionally, since the masses of the two pendula are equal, the other two parameters for the coupled systems (τ_1 and τ_2) should be approximately equal, which is the case as well. Note that these parameters can only be estimated up to a certain scaling, as changing the masses or the position of the spring's attachment point has the same effect on the dynamics as changing the spring stiffness.

We can compare the natural frequencies of the dynamical systems using the estimated dynamical parameters as in (38) to the frequency spectrum of the reference line used for validation. As can be seen in Fig. 7, the locations of the natural frequencies correspond well to the peaks in the zero-padded FFT spectrum. This indicates that the estimated dynamical parameters are accurately identified, and can be used to predict the dynamics of the systems.

Finally, the RMSE_x values and estimated lengths for the retrospectively undersampled data can be seen in Table 4. Even with only 2 sample points per readout, the dynamics could still be determined, albeit with a slightly larger error compared to the reference. Fig. 8 shows that the displacements estimated from undersampled data can barely be distinguished from the ones estimated from fully sampled data. This indicates that reconstruction using the spectro-dynamic MRI model is possible with extremely high undersampling rates.

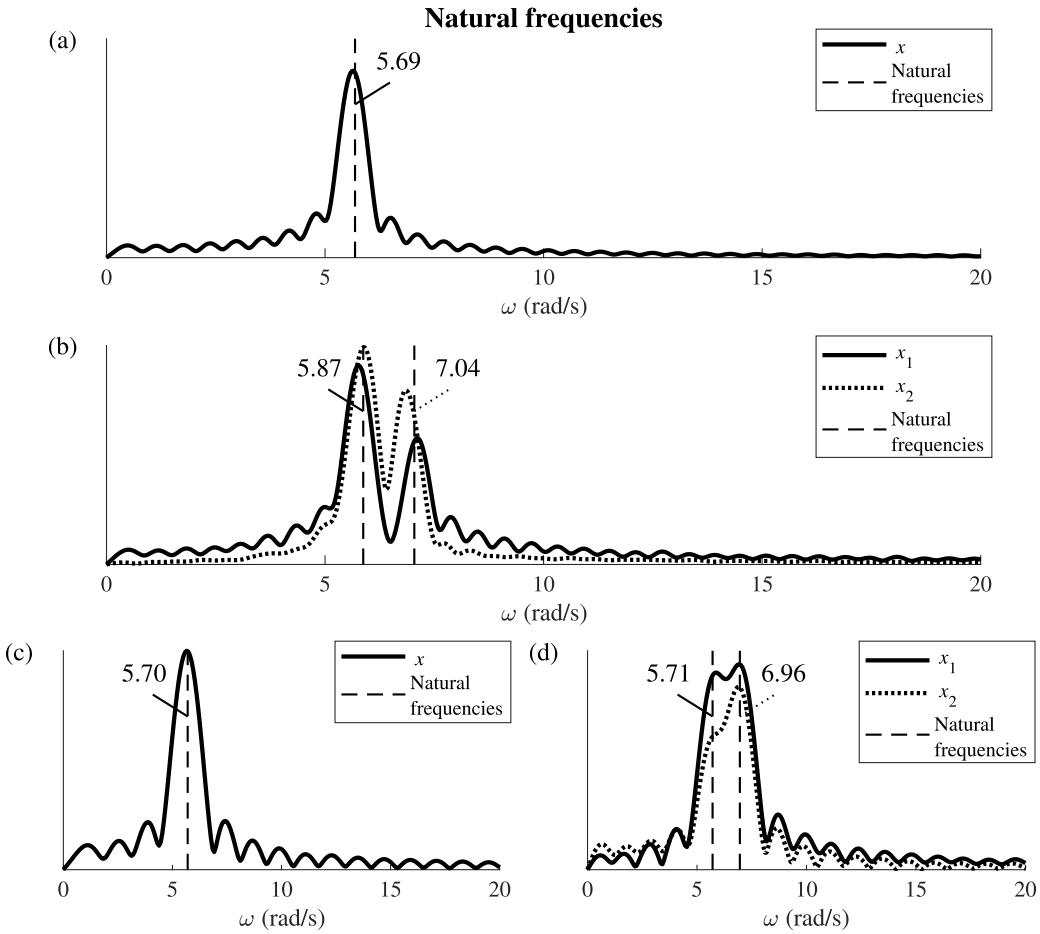

FIGURE 7. Natural frequencies of the estimated systems for the experiments with (a) a simple pendulum, (b) coupled pendula, (c) a spherical pendulum, and (d) coupled spherical pendula. The plotted spectra are the temporal FFTs of the validation data, as determined in Fig. 5, which is regarded as reference data. The black dashed vertical lines indicate the natural frequencies for each system as calculated from the dynamical model by (38), using the estimated dynamical parameters θ.

V. DISCUSSION

We have introduced spectro-dynamic MRI as a method for the identification of dynamical systems from MRI measurements at a very high temporal resolution. A measurement model has been derived to connect the measured data to the motion fields. By using the measured data directly in k-space, a temporal resolution of a few milliseconds could be achieved, without assuming any periodicity in the motion pattern. To handle highly undersampled data, a dynamical model has been added as a regularization term. These two models were optimized simultaneously to estimate the displacement field, as well as a set of dynamical system parameters. Our proposed method has been validated on four simple systems, and we have shown that it is possible to accurately estimate both 1D and 2D dynamics with only two data points per readout.

The estimated displacements in Fig. 6 correspond well to the reference motion fields, with an RMSE_x of less than 1.3 mm in all experiments. When comparing these results to those obtained from data acquired with a conventional linear ordering, as in Fig. 1(a), the advantage of using the proposed spectro-dynamic ordering becomes clear (see Fig. S1).

Note that the amplitude of the reconstructed displacements gradually decreases. This is caused by the friction of the pendula. Even though no friction force has been included in the dynamical model, this phenomenon could still be reconstructed from the data through the measurement model together with the correct dynamical parameters. This shows the importance of the trade-off coefficient λ in (20), as dynamical model imperfections can still be reconstructed when its value has been chosen correctly. Furthermore, this allows the model to handle discontinuous motion, as shown in Fig. S2.

The sampling pattern can have a large effect on the results of the reconstruction. We used a Cartesian sampling pattern, with one readout line per time point. Thus, the measurements are intrinsically undersampled in the phase-encode direction, as only a single k_y-coordinate is sampled during every readout. As a result, the motion along the readout direction could be estimated more accurately. The accuracy of the estimated

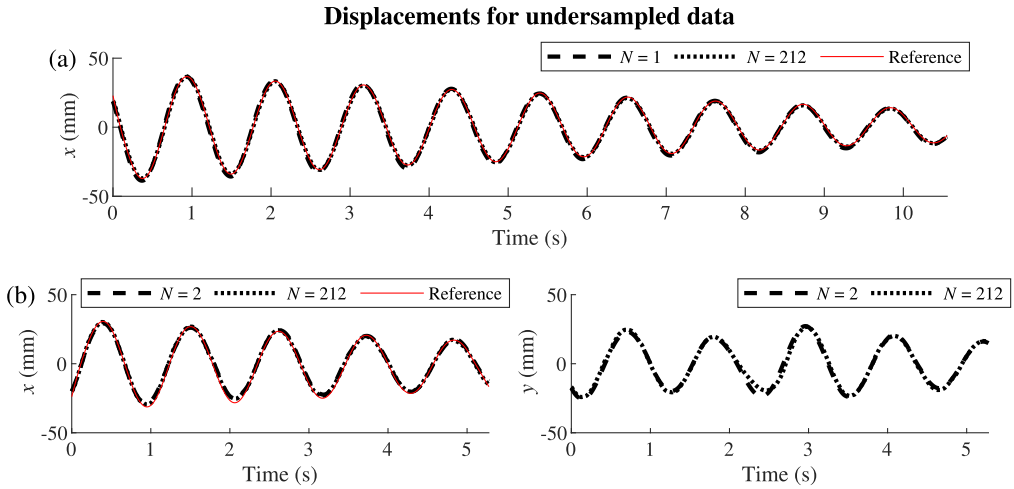

FIGURE 8. The estimated displacements for the undersampled datasets of (a) a simple pendulum, and (b) a spherical pendulum. The red line is the reference line as computed by the spatial 1D FFTs of the readouts shown in Fig. 5. Note how the estimated displacements with only one or two samples every readout are almost identical to those estimated with all 212 samples in the readout direction. This indicates that our method is robust against high undersampling.

TABLE 4. Undersampled reconstruction.

Samples per readout	Simple Pendulum		Spherical Pendulum	
	RMSE_x [mm]	l [mm]	RMSE_x [mm]	l [mm]
212	0.43	303	1.3	302
40	0.43	303	1.3	302
20	0.50	304	1.4	302
10	0.62	304	1.4	306
4	0.64	306	1.6	305
2	0.73	308	1.7	308
1	1.4	308	N.A.[1]	N.A.[1]

[1]Estimating the displacements in both directions is not possible with one measurement.

displacements was dependent on which k_y-coefficient was sampled. For most objects, most of the energy of the signal is located around the center of k-space where the low spatial frequencies are sampled, while the noise is distributed evenly over the entire k-space. Sampling at high spatial frequencies thus results in a low signal-to-noise ratio (SNR). On the other hand, at very low spatial frequencies, only global intensity changes are encoded, which are less sensitive to small displacements. This can be seen in the distribution of the spatial derivative in the spectral domain (Section S.II and Fig. S3). Therefore, most of the useful information about the dynamics is located at those spatial frequencies with a sufficiently high level of detail, while still having sufficient SNR.

Since our data consisted of a single measurement in the phase-encode direction, the convolution in (10) cannot be performed in this dimension. The basis functions used in this work did not have a dependency on the y-coordinate and therefore this problem was circumvented. However, the convolution must be evaluated correctly for systems where this is no longer the case. One possible solution would be to iteratively reconstruct the motion fields together with the missing data, enabling the calculation of the convolution.

Other sampling patterns could give better coverage of k-space while still capturing the dynamic information. For example, spiral or EPI trajectories can sample both low and high spatial frequencies in both directions during a single readout. Optimizing these trajectories could result in a better trade-off between SNR and spatial resolution, thus enhancing the efficiency of the proposed method. However, not all sampling patterns are suitable to be used for spectro-dynamic MRI. A radial acquisition scheme cannot be used for example, since it would introduce a linear dependency between the k-space coordinates in (10). As a result, the matrix A in (20) would become rank-deficient, creating an ill-conditioned inversion problem and making it impossible to estimate the displacements in all directions simultaneously. This also occurs in a Cartesian acquisition when sampling the $k_y = 0$ line, where the displacements in the y-direction cannot be estimated. In Fig. 6(c) and 6(d), the estimated y-displacements during the acquisition of these samples are solely based on the dynamical model, effectively interpolating the dynamics between the closest surrounding points for which $k_y \neq 0$. Investigating which sampling patterns are efficient for spectro-dynamic MRI will be the topic of future research. For some preliminary results of simulations with radial and spiral sampling patterns, see Section S.I and Fig. S4.

Another option would be to use an interleaved sampling pattern by sampling not one but a few different phase-encode coefficients, after which this pattern is repeated. This can be seen as a hybrid between Fig. 1(a) and 1(b). An interleaved pattern will increase the amount of data sampled per time interval, at the cost of a larger Δt. With a few interleaved phase-encoding steps, this decrease in temporal resolution

will likely remain acceptable. This can also provide a possible way to calculate the convolution in the measurement model by sampling several consecutive phase-encode lines and assuming that the displacement field is smooth and continuous in this direction.

The spectro-dynamic MRI model is generic and can be applied to 3D experiments. However, this will increase the effective undersampling factor since there are two phase-encode directions (k_y and k_z). By retrospectively undersampling the 2D experimental data down to only 2 samples per readout, we have shown that there is still room for further reduction in the number of sampling points. This robustness against undersampling is promising for future extensions of spectro-dynamic MRI to 3D acquisitions. Optionally, more regularization can be added to the displacement fields, as is done in image registration [37]. Prior knowledge about the dynamical parameters can also be added to regularize the reconstruction. Finally, replacing the body coil with an array coil and incorporating the sensitivity fields in the measurement model can help to further increase the undersampling factor [25].

Currently, the error of (18) is minimized using ordinary least squares, implicitly assuming that only the vector $\mathbf{b}$ is subject to noise. However, the measurements are also used to construct the matrix A, thereby introducing errors in this matrix as well. A total least squares method [36], [38] would be required to take the systematic errors in the matrix A, caused by measurement imperfections, into account during the minimization of (20). This makes the optimization more complex, but it could result in a better estimation of the dynamics.

The dynamical systems investigated in this work were all constructed using nondeformable objects. As a result, the third term in the measurement model (10), originating from the divergence of the velocity field, is always equal to zero. However, as soon as an object is deforming, the divergence of the velocity field can become nonzero, and this term of the measurement model must be taken into account. We have seen in numerical simulations (shown in Fig. S5) that the omission of this term leads to a significant error in the estimated displacements when the simulated divergence is nonzero. In the future, we would like to perform additional experiments with more complex dynamics, and deformable systems in particular, to verify the spectro-dynamic MRI method when the displacement fields are no longer piecewise constant.

Spectro-dynamic MRI could enable the identification of dynamical systems, such as the heart or the motion of joints, in vivo at a high temporal resolution. Although the measurement model does not depend on the system under investigation, additional effects such as static or RF field inhomogeneities could play a role in biological systems. Further research will determine the best way to deal with these complications in more complex setups.

Furthermore, the dynamical model would need to be adjusted to model deformable organ tissues with different dynamical parameters. Deriving such a model from first principles, as was done for the simple systems in this work, is challenging and would result in complex models with many parameters. This would make it extremely difficult to estimate these parameters without overfitting, as well as analyzing these complex systems once a proper model has been found. As an alternative, data-driven discovery of dynamical systems [39]–[41] can be applied to learn the dynamics directly from the observed data. These methods generate phenomenological models with reduced complexity compared to those derived from first principles, while still being able to capture complex dynamics. Using this data-driven approach, prior information about cardiac or musculoskeletal dynamics can be introduced in the spectro-dynamic MRI framework. Addressing this challenge will be the topic of future research.

VI. CONCLUSION

We have developed spectro-dynamic MRI as a method that makes the identification of dynamical systems possible at a high temporal resolution of a few milliseconds. The measurements in k-space were connected to the displacement field through a measurement model. Adding the dynamical model allowed for the reconstruction of the displacement fields and the dynamical parameters of the system. We have experimentally shown that spectro-dynamic MRI can accurately reconstruct the dynamics of simple systems, even with very high undersampling factors.

APPENDIX A
CONSERVATION OF MAGNETIZATION

To derive (6), we start by looking at the volume integral of the transverse magnetization over an arbitrary volume element $V_0 \in \mathbb{R}^3$. This control volume is fixed in space, while the object is moving. The rate of change of the magnetization within V_0 is equal to the inflow of magnetization across the surface S_0 of this volume element:

$$\frac{d}{dt}\iiint_{V_0} m(\mathbf{r},t)\,dV + \oiint_{S_0} m(\mathbf{r},t)\mathbf{v}(\mathbf{r},t)\cdot\mathbf{n}\,dS = 0. \quad (39)$$

Here $\mathbf{v}(\mathbf{r},t)$ is the velocity field, and $\mathbf{n}$ is the unit normal vector of the surface element. Because our volume element is not moving, we can move the temporal derivative inside the integral:

$$\frac{d}{dt}\iiint_{V_0} m(\mathbf{r},t)\,dV = \iiint_{V_0} \frac{\partial}{\partial t} m(\mathbf{r},t)\,dV. \quad (40)$$

Furthermore, we can use the divergence theorem:

$$\oiint_{S} \big[m(\mathbf{r},t)\mathbf{v}(\mathbf{r},t)\big]\cdot\mathbf{n}\,dS = \iiint_{V} \nabla\cdot\big[m(\mathbf{r},t)\mathbf{v}(\mathbf{r},t)\big]\,dV. \quad (41)$$

Combining (39), (40), and (41), we can write the measurement model in integral form:

$$\iiint_{V_0} \frac{\partial}{\partial t} m(\mathbf{r},t)\,dV + \iiint_{V_0} \nabla\cdot\big[m(\mathbf{r},t)\mathbf{v}(\mathbf{r},t)\big]\,dV = 0. \quad (42)$$

Since (42) must hold for any V_0, we can extract the integrand and rewrite our measurement model in the differential form:

$$\frac{\partial}{\partial t} m(\mathbf{r}, t) + \nabla \cdot \left[m(\mathbf{r}, t) \mathbf{v}(\mathbf{r}, t) \right] = 0. \tag{43}$$

APPENDIX B
VELOCITY FIELD APPROXIMATION

Assume we have an object in a certain reference configuration at time t_0. The location of one specific particle within this object at t_0 is $\mathbf{r}_0$. As this object moves through space, the location $\mathbf{r}$ of this particle changes. The displacement field is a function of both space and time. It can be written as a function of the location of each particle in the reference configuration, called the Lagrangian description, where the initial location $\mathbf{r}_0$ is an independent variable:

$$\mathbf{u}(\mathbf{r}_0, t) = \mathbf{r}(\mathbf{r}_0, t) - \mathbf{r}_0. \tag{44}$$

Alternatively, we can use the Eulerian description of the displacement field, in which the current coordinate is used as independent variable:

$$\mathbf{u}(\mathbf{r}, t) = \mathbf{r} - \mathbf{r}_0(\mathbf{r}, t). \tag{45}$$

Notice that the initial coordinate of the particle is now no longer an independent variable, but it has become a function of the current coordinate. Both descriptions can be used to describe the same displacement field, but the Lagrangian description "follows" the same particles over time, while in the Eulerian description, the displacements are always described with respect to the same static spatial coordinates.

Since the magnetization is measured at fixed coordinates, it is more convenient to use the Eulerian description for the displacement field in the measurement model, as is done in Section II-C. This requires an Eulerian expression of the velocity field as well.

The velocity field is the rate of change in the position of each particle. That means we need to keep $\mathbf{r}_0$ constant when taking the temporal derivative:

$$\mathbf{v} = \left. \frac{d\mathbf{r}}{dt} \right|_{\mathbf{r}_0 = \text{constant}} \equiv \frac{D\mathbf{r}}{Dt}. \tag{46}$$

Here, $\frac{D}{Dt}$ is the material derivative [42]. When the Lagrangian description as in (44) is used, the velocity field can be readily obtained from the displacement field:

$$\mathbf{v}(\mathbf{r}_0, t) = \frac{D}{Dt} \mathbf{u}(\mathbf{r}_0, t) = \frac{\partial}{\partial t} \mathbf{u}(\mathbf{r}_0, t). \tag{47}$$

However, for the Eulerian description as in (45), the total derivative with respect to time must be taken:

$$\begin{aligned} \mathbf{v}(\mathbf{r}, t) &= \frac{D}{Dt} \mathbf{u}(\mathbf{r}, t) \\ &= \frac{\partial}{\partial t} \mathbf{u}(\mathbf{r}, t) + \nabla \mathbf{u}(\mathbf{r}, t) \cdot \frac{d\mathbf{r}}{dt} \\ &= \frac{\partial}{\partial t} \mathbf{u}(\mathbf{r}, t) + \nabla \mathbf{u}(\mathbf{r}, t) \cdot \mathbf{v}(\mathbf{r}, t). \end{aligned} \tag{48}$$

Solving for $\mathbf{v}(\mathbf{r}, t)$ gives us an expression for the velocity field in the current configuration:

$$\mathbf{v}(\mathbf{r}, t) = (I - \nabla \mathbf{u}(\mathbf{r}, t))^{-1} \frac{\partial}{\partial t} \mathbf{u}(\mathbf{r}, t), \tag{49}$$

where I is the identity matrix.

When the deformation of the moving object is small, $\nabla \mathbf{u}(\mathbf{r}, t)$ is small as well. Note that this assumption does not limit the displacements themselves, only the spatial derivative of the displacement field. In this case, the velocity field can be approximated as the partial temporal derivative of the displacement field in the Eulerian description:

$$\mathbf{v}(\mathbf{r}, t) \approx \frac{\partial}{\partial t} \mathbf{u}(\mathbf{r}, t). \tag{50}$$

This assumption allows us to express the measurement model as a linear function of the displacement field, as can be seen in (9).

ACKNOWLEDGMENT

The authors would like to thank Prof. Nico van den Berg and Tom Bruijnen for their help and advice regarding the execution of the experiments and the analysis of the data.

REFERENCES

[1] G. Savarese and L. H. Lund, "Global public health burden of heart failure," *Cardiac Failure Rev.*, vol. 3, no. 1, pp. 7–11, 2017.
[2] J. J. Atherton, J. Bauersachs, and S. Carerj, "2016 ESC guidelines for the diagnosis and treatment of acute and chronic heart failure," *Eur. Heart J.*, vol. 37, no. 27, pp. 2129–2200, 2016.
[3] M. S. Amzulescu, M. De Craene, H. Langet, A. Pasquet, D. Vancraeynest, A. C. Pouleur, J. L. Vanoverschelde, and B. L. Gerber, "Myocardial strain imaging: Review of general principles, validation, and sources of discrepancies," *Eur. Heart J.-Cardiovascular Imag.*, vol. 20, no. 6, pp. 605–619, Jun. 2019.
[4] A. D. Woolf and B. Pflege, "Burden of major musculoskeletal conditions," *Bull. World Health Org.*, vol. 81, no. 9, pp. 646–656, 2003.
[5] L. M. Shapiro and G. E. Gold, "MRI of weight bearing and movement," *Osteoarthritis Cartilage*, vol. 20, no. 2, pp. 69–78, Feb. 2012, doi: 10.1016/j.joca.2011.11.003.
[6] R. W. Brown, Y.-C. N. Cheng, E. M. Haacke, M. R. Thompson, and R. Venkatesan, *Magnetic Resonance Imaging: Physical Principles and Sequence Design*, 2nd ed. Hoboken, NJ, USA: Wiley, 2014.
[7] L. Axel and R. Otazo, "Accelerated MRI for the assessment of cardiac function," *Brit. J. Radiol.*, vol. 89, no. 1063, Jul. 2016, Art. no. 20150655.
[8] A. B. Kerr, J. M. Pauly, B. S. Hu, K. C. Li, C. J. Hardy, C. H. Meyer, A. Macovski, and D. G. Nishimura, "Real-time interactive MRI on a conventional scanner," *Magn. Reson. Med.*, vol. 38, no. 3, pp. 355–367, Sep. 1997.
[9] M. Uecker, S. Zhang, D. Voit, A. Karaus, K.-D. Merboldt, and J. Frahm, "Real-time MRI at a resolution of 20 ms," *NMR Biomed.*, vol. 23, no. 8, pp. 986–994, 2010.
[10] D. J. Atkinson and R. R. Edelman, "Cineangiography of the heart in a single breath hold with a segmented turboFLASH sequence," *Radiology*, vol. 178, no. 2, pp. 357–360, 1991.
[11] A. C. Larson, R. D. White, G. Laub, E. R. McVeigh, and D. Li, "Self-gated cardiac cine MRI," *Magn. Reson. Med.*, vol. 51, no. 1, pp. 93–102, Jan. 2004.
[12] K. P. Pruessmann, M. Weiger, M. B. Scheidegger, and P. Boesiger, "SENSE: Sensitivity encoding for fast MRI," *Magn. Reson. Med.*, vol. 42, no. 5, pp. 952–962, Jul. 1999.
[13] M. A. Griswold, P. M. Jakob, R. M. Heidemann, M. Nittka, V. Jellus, J. Wang, B. Kiefer, and A. Haase, "Generalized autocalibrating partially parallel acquisitions (GRAPPA)," *Magn. Reson. Med.*, vol. 47, no. 6, pp. 1202–1210, 2002.
[14] M. Lustig, D. Donoho, and J. M. Pauly, "Sparse MRI: The application of compressed sensing for rapid MR imaging," *Magn. Reson. Med.*, vol. 58, no. 6, pp. 1182–1195, Oct. 2007.

[15] K. G. Hollingsworth, "Reducing acquisition time in clinical MRI by data undersampling and compressed sensing reconstruction," *Phys. Med. Biol.*, vol. 60, no. 21, pp. R297–R322, 10 2015.
[16] J. P. Haldar and Z. P. Liang, "Spatiotemporal imaging with partially separable functions: A matrix recovery approach," in *Proc. Int. Symp. Biomed. Imag., From Nano to Macro*, 2010, pp. 716–719.
[17] K. T. Block, H. Chandarana, S. Milla, M. Bruno, T. Mulholland, G. Fatterpekar, M. Hagiwara, R. Grimm, C. Geppert, B. Kiefer, and D. K. Sodickson, "Towards routine clinical use of radial stack-of-stars 3D gradient-echo sequences for reducing motion sensitivity," *J. Korean Soc. Magn. Reson. Med.*, vol. 18, no. 2, pp. 87–106, 2014.
[18] M. Zaitsev, J. Maclaren, and M. Herbst, "Motion artifacts in MRI: A complex problem with many partial solutions," *J. Magn. Reson. Imag.*, vol. 42, no. 4, pp. 887–901, Oct. 2015.
[19] L. Feng, R. Grimm, K. T. Block, H. Chandarana, S. Kim, J. Xu, L. Axel, D. K. Sodickson, and R. Otazo, "Golden-angle radial sparse parallel MRI: Combination of compressed sensing, parallel imaging, and golden-angle radial sampling for fast and flexible dynamic volumetric MRI," *Magn. Reson. Med.*, vol. 72, no. 3, pp. 707–717, 2014.
[20] R. Otazo, E. J. Candès, and D. K. Sodickson, "Low-rank plus sparse matrix decomposition for accelerated dynamic MRI with separation of background and dynamic components," *Magn. Reson. Med.*, vol. 73, no. 3, pp. 1125–1136, 2014.
[21] L. Feng, L. Axel, H. Chandarana, K. T. Block, D. K. Sodickson, and R. Otazo, "XD-GRASP: Golden-angle radial MRI with reconstruction of extra motion-state dimensions using compressed sensing," *Magn. Reson. Med.*, vol. 75, no. 2, pp. 775–788, 2016.
[22] F. Ong, X. Zhu, J. Y. Cheng, K. M. Johnson, P. E. Z. Larson, S. S. Vasanawala, and M. Lustig, "Extreme MRI: Large-scale volumetric dynamic imaging from continuous non-gated acquisitions," *Magn. Reson. Med.*, vol. 84, no. 4, pp. 1763–1780, Oct. 2020.
[23] F. Odille, P.-A. Vuissoz, P.-Y. Marie, and J. Felblinger, "Generalized reconstruction by inversion of coupled systems (GRICS) applied to free-breathing MRI," *Magn. Reson. Med.*, vol. 60, no. 1, pp. 146–157, Jul. 2008.
[24] N. R. F. Huttinga, C. A. T. van den Berg, P. R. Luijten, and A. Sbrizzi, "MR-MOTUS: Model-based non-rigid motion estimation for MR-guided radiotherapy using a reference image and minimal K-space data," *Phys. Med. Biol.*, vol. 65, no. 1, Jan. 2020, Art. no. 015004.
[25] N. R. F. Huttinga, T. Bruijnen, C. A. T. van den Berg, and A. Sbrizzi, "Non-rigid 3D motion estimation at high temporal resolution from prospectively undersampled K-space data using low-rank MR-MOTUS," *Magn. Reson. Med.*, vol. 85, no. 4, pp. 2309–2326, Apr. 2020.
[26] T. van Leeuwen and F. J. Herrmann, "A penalty method for PDE-constrained optimization in inverse problems," *Inverse Problems*, vol. 32, no. 1, pp. 1–26, 2016.
[27] P. K. Kundu and I. M. Cohen, *Fluid Mechanics*, 4th ed. Burlington, MA, USA: Academic, 2008.
[28] B. de Kraker and D. H. van Campen, *Mechanical Vibrations*. Maastricht, The Netherlands: Shaker, 2001.
[29] J. He and Z.-F. Fu, *Modal Analysis*. Oxford, U.K.: Butterworth-Heinemann, 2001.
[30] T. L. Schmitz and K. S. Smith, *Mechanical Vibrations: Modeling and Measurement*. Boston, MA, USA: Springer, 2012.
[31] M. G. Olsson, "Spherical pendulum revisited," *Amer. J. Phys.*, vol. 49, no. 6, pp. 531–534, 1981.
[32] P. C. Hansen, "Regularization tools: A MATLAB package for analysis and solution of discrete ill-posed problems," *Numer. Algorithms*, vol. 6, pp. 1–35, Mar. 1998.
[33] G. H. Golub and V. Pereyra, "The differentiation of pseudo-inverses and nonlinear least squares problems whose variables separate," *SIAM J. Numer. Anal.*, vol. 10, no. 2, pp. 413–432, Feb. 1973.
[34] G. Golub and V. Pereyra, "Separable nonlinear least squares: The variable projection method and its applications," *Inverse Problems*, vol. 19, no. 2, pp. R1–R26, Apr. 2003.
[35] D. P. O'Leary and B. W. Rust, "Variable projection for nonlinear least squares problems," *Comput. Optim. Appl.*, vol. 54, no. 3, pp. 579–593, 2013.
[36] G. H. Golub and C. F. Van Loan, *Matrix Computations*, 4th ed. Batlimore, MD, USA: John Hopkins Univ. Press, 2013.
[37] B. Fischer and J. Modersitzki, "Ill-posed medicine—An introduction to image registration," *Inverse Problems*, vol. 24, no. 3, Jun. 2008, Art. no. 034008.
[38] I. Markovsky and S. Van Huffel, "Overview of total least-squares methods," *Signal Process.*, vol. 87, no. 10, pp. 2283–2302, 2007.
[39] B. C. Daniels and I. Nemenman, "Automated adaptive inference of phenomenological dynamical models," *Nature Commun.*, vol. 6, pp. 1–8, Dec. 2015.
[40] S. L. Brunton and J. N. Kutz, *Data-Driven Science and Engineering*. Cambridge, U.K.: Cambridge Univ. Press, 2019.
[41] S. H. Rudy, J. N. Kutz, and S. L. Brunton, "Deep learning of dynamics and signal-noise decomposition with time-stepping constraints," *J. Comput. Phys.*, vol. 396, pp. 483–506, 2019, doi: 10.1016/j.jcp.2019.06.056.
[42] F. Irgens, *Continuum Mechanics*. Berlin, Germany: Springer, 2008.

MAX H. C. VAN RIEL was born in Tilburg, The Netherlands, in 1998. He received the B.Sc. degree in biomedical engineering from the Eindhoven University of Technology, in 2018, the master's degree in medical imaging from the Eindhoven University of Technology, and the M.Sc. degree form the University Medical Center Utrecht, in 2020, where he is currently pursuing the Ph.D. degree.

In 2019, he was a Student Intern at NYU Langone Health for six months. Under the supervision of Martijn A. Cloos, he worked on implementing a free-breathing MR fingerprinting method for quantitative abdominal imaging.

Mr. van Riel was awarded the Young Talent Award from the Royal Holland Society of Sciences and Humanities in 2016.

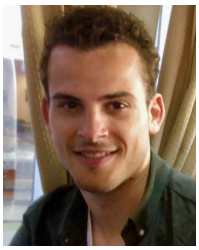

NIEK R. F. HUTTINGA received the B.S. and M.S. degrees in applied mathematics from the University of Twente, Enschede, The Netherlands, with a specialization in mathematical physics, in 2014 and 2017, respectively. He is currently pursuing the Ph.D. degree in applied mathematics with the Computational Imaging Group, UMC Utrecht, Utrecht, The Netherlands, under supervision of Dr. Alessandro Sbrizzi, and Prof. Dr. Nico van den Berg.

His previous research projects focused on computational fluid dynamics, and theory and applications of deep learning. His current research interests include motion reconstruction for MRI and radiotherapy (MR-MOTUS), mathematical modeling, and deep learning.

Mr. Huttinga received two merit awards from the International Society for Magnetic Resonance Imaging (ISMRM) for his work on MR-MOTUS: 1x top 3% of submitted abstracts and 1x top 15% of submitted abstracts. Additionally, he received the Best Power-Poster Award at the ISMRM Benelux Conference 2020, and the Best Oral Presentation Award at the Study Group for MR-Guided Radiotherapy at the ISMRM Conference 2019.

ALESSANDRO SBRIZZI received the Ph.D. degree in mathematics from the Utrecht University, in 2013, with a thesis focused on modeling and numerical optimization of MRI acquisition and reconstruction processes.

He is currently an Associate Professor at the Computational Imaging Group, UMC Utrecht. His research interests include fast multi-parametric MRI (in particular MR-STAT), real-time motion-estimation (MR-MOTUS technique), radiofrequency pulse design, and the application of machine learning in MRI.

Dr. Sbrizzi was a recipient of an NWO-VENI Grant (2016–2021), an NWO-Demonstrator Grant (2018-02020), and an NWO-HTSM Grant (2020–2024) as a Principal Investigator.